

## Chapter 4

### Shear Rate Dependence of Pressure, Energy and Viscosity in Planar Couette Flow

In this chapter, NEMD simulations of the shear viscosity of argon and xenon are presented. In the simulations with argon, the atoms interact via the Barker-Fisher-Watts (BFW) [Bar71a] and Axilrod-Teller (AT) [Axi43] intermolecular potentials (see Chapter 2). In the simulations with xenon, the atoms interact via the potential devised by Barker et al. [Bar74] and Axilrod-Teller (AT) [Axi43] potentials (see Chapter 2). An adequate system size of 500 atoms was used, resulting in greater statistical accuracy than reported elsewhere [Lee93, Lee94]. We show that the pressure is clearly not a linear function of  $\dot{\mathbf{g}}^{3/2}$ , but can be described by an analytic  $\dot{\mathbf{g}}^2$  dependence. This relationship is independent of the three-body potential interaction and is only a consequence of two-body interactions. Our results also demonstrate that the shear viscosity is not necessarily a linear function of  $\dot{\mathbf{g}}^{1/2}$ . The statistical accuracy of the viscosity data is however not sufficient to unambiguously determine an accurate dependence on the strain rate. In section 4.1 we give the details of the simulations performed and report the results in section 4.2. In section 4.3 we analyze for the non-equilibrium case the ratio between the three-body energy and two-body energy as done in section 3.2.

## 4.1 Simulation details

### NEMD Algorithm

The NEMD simulations were performed by applying the standard SLLOD equations of motion for planar Couette flow (see Chapter 2). The SLLOD equations for a one-component atomic fluid flowing with streaming velocity  $v_x$  in the  $x$ -direction and constant strain rate  $\dot{\mathbf{g}} = \frac{dv_x}{dy}$  were applied (see Eq. 2.72 and Eq. 2.77). The equations of motion were integrated by a 4<sup>th</sup> order Gear predictor-corrector scheme (see Chapter 2), with a reduced integration time step ( $t^* = t\sqrt{\mathbf{e}/m\mathbf{s}^2}$ ) of 0.001. A non-equilibrium simulation trajectory is typically run for 250000 time steps. To equilibrate the system, each trajectory is first run without a shearing field. After the shearing field is switched on, the first 50000 time steps of each trajectory are ignored, and the fluid is allowed to relax to a non-equilibrium steady-state. In the simulations with argon atoms averages were taken over 5 independent trajectories, each starting at a new configuration. Thus, every pressure, energy and viscosity data point represents a total run length of  $5 \times 200000 = 10^6$  time steps. In the simulations with xenon, averages are taken over 2 independent trajectories, resulting in the same statistical accuracy.

### Intermolecular potentials

The total intermolecular potential adopted consists in contributions from two-body interactions ( $u_{2b}$ ) and three-body dispersion interactions ( $u_{3b}$ ). As previously mentioned, for argon we used BFW + AT potentials and for xenon Barker et al. [Bar74] + AT potentials. The two-body potentials were truncated at half the box length and appropriate long-range correction terms were evaluated to recover the contribution to

the pressure and energy for the full intermolecular potential (see Appendix 1). The three-body potentials were truncated at a quarter of the box length (see Appendix 2) and the long-range correction terms for energy and pressure were evaluated as:

$$E_{3b}^{Long-range} = N\mathbf{r}^2 \iint_{\substack{r_{12} < r_{13} < r_{23} \\ r_{23} > r_{3b}^{cut-off}}} g^{(3)}(r_{12}, r_{13}, r_{23}) u_{3b}(r_{12}, r_{13}, r_{23}) dr_{12} dr_{13} \quad (4.1)$$

where  $g^{(3)}(r_{12}, r_{13}, r_{23})$  is the 3<sup>rd</sup> order radial distribution function written as:

$$g^{(3)}(r_{12}, r_{13}, r_{23}) = g^{(2)}(r_{12})g^{(2)}(r_{13})g^{(2)}(r_{23}) \quad (4.2)$$

using the superposition approximation [Bar71a] and setting  $g^{(2)}(r_{23})$  to unity.

The long-range correction for the three-body pressure was calculated as:

$$P_{3b}^{Long-range} = \frac{3E_{3b}^{Long-range}}{V} \quad (4.3)$$

where we used the fact that the Axilord-Teller potential is a homogeneous function [Bar71a, see also Appendix 2].

Before applying the SLLOD algorithm using these intermolecular potentials, we repeated simulations on a Lennard-Jones (LJ) fluid at the LJ triple point ( $T^* = 0.722$ ,  $\mathbf{r}^* = 0.8442$ , where the superscript \* stands for reduced units), reported by Evans et al. [Eva89]. Our simulations were in excellent agreement with these results, and are displayed in Figures 4.1, 4.2 and 4.3. The pressures and energies were found to vary linearly with  $\dot{\mathbf{g}}^{3/2}$ , whereas the viscosity varied as  $\dot{\mathbf{g}}^{1/2}$ , as previously observed. We further note that all subsequent simulations performed on the BFW + AT and BWLSL + AT fluids are made with *exactly* the same computer program. The only difference is the form of the intermolecular potentials, and hence forces, used in the calculation of fluid properties. This limits any possible errors that could be introduced by comparing results generated from different code.

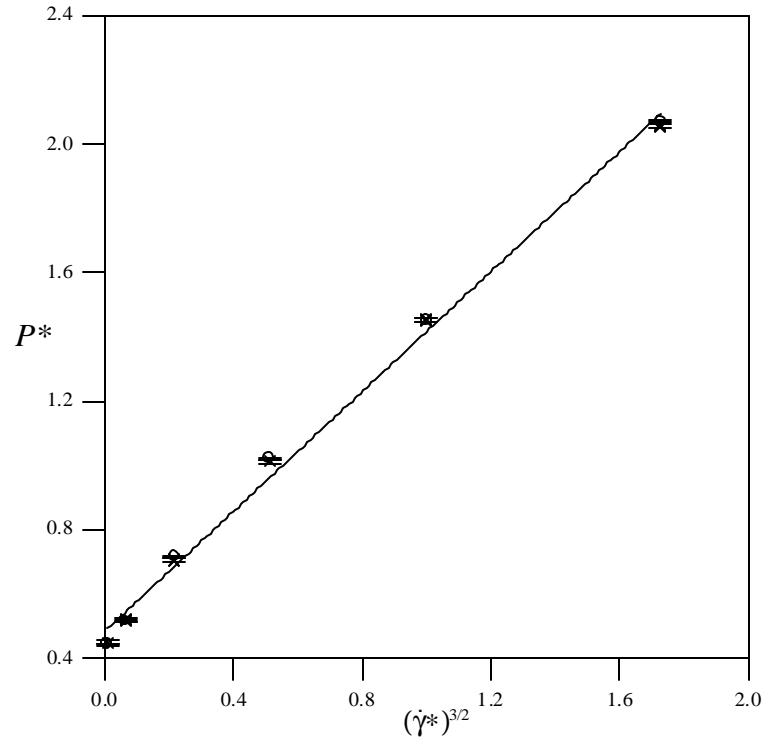


Figure 4.1 Comparison of Evans et al. [Eva89] pressure ( $\circ$ ) with our own ( $\times$ ) for a system of 2048 Lennard-Jones atoms and a cut-off  $=3.5$  (reduced units).

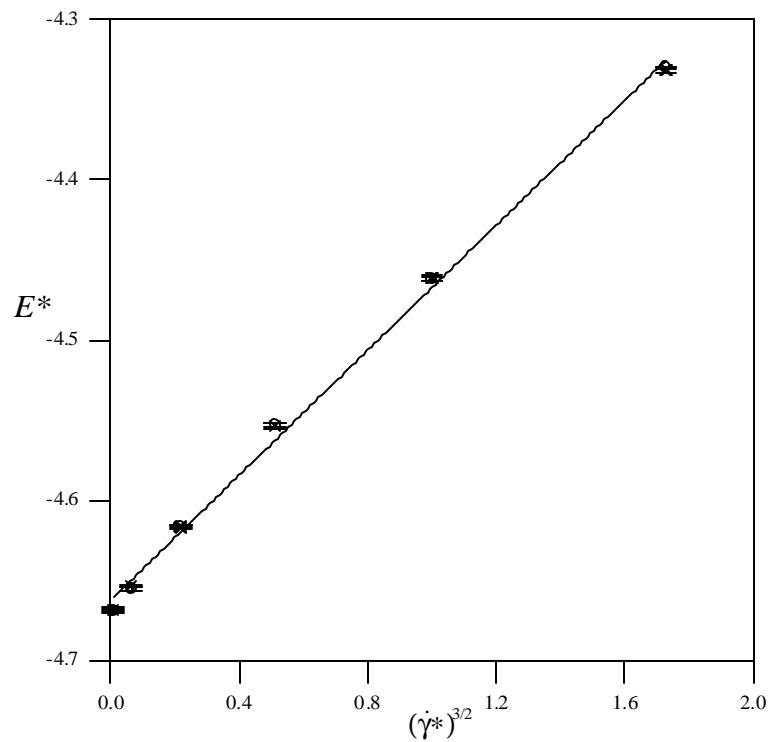


Figure 4.2 Comparison of Evans et al. [Eva89] configurational energy ( $\circ$ ) with our own ( $\times$ ) for a system of 2048 Lennard-Jones atoms and a cut-off  $=3.5$  (reduced units).

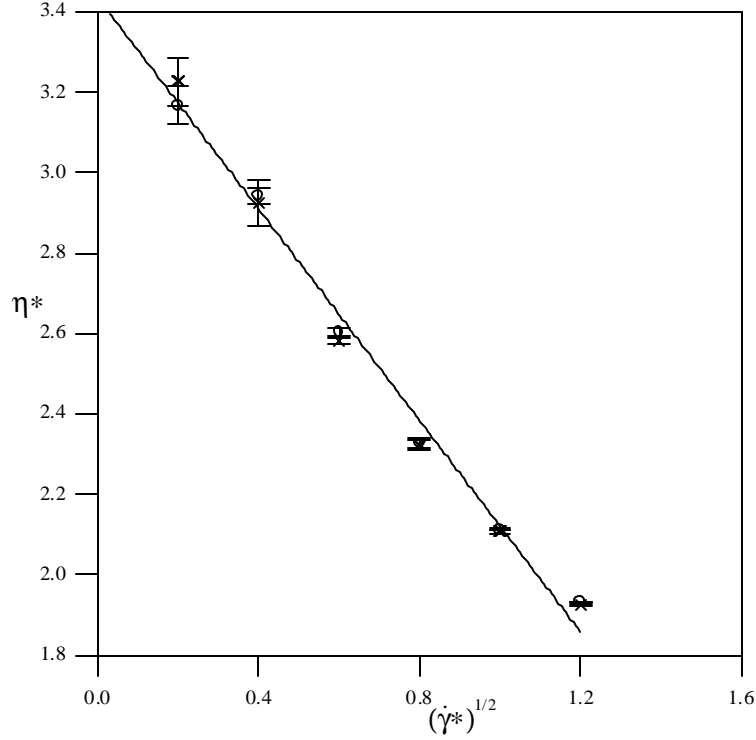


Figure 4.3 Comparison of Evans et al. [Eva89] viscosity ( $\circ$ ) with our own ( $\times$ ) for a system of 2048 Lennard-Jones atoms and a cut-off  $=3.5$  (reduced units).

## 4.2 Results

The results of the NEMD simulations for the pressure, energy and shear viscosity of argon at different strain rates are reported in Table 4.1. Results for xenon are reported in Table 4.2. The normal convention was adopted for the reduced density ( $\mathbf{r}^* = \mathbf{r}\mathbf{s}^3$ ), temperature ( $T^* = kT/\mathbf{e}$ ), energy ( $E^* = E/\mathbf{e}$ ), pressure ( $P^* = P\mathbf{s}^3/\mathbf{e}$ ), viscosity ( $\mathbf{h}^* = \mathbf{h}\mathbf{s}^2(m\mathbf{e})^{-1/2}$ ) and strain rate ( $\mathbf{g}^* = \dot{\mathbf{g}}[\mathbf{s}(m/\mathbf{e})^{1/2}]$ ). All simulations for argon were performed at the state point  $(\mathbf{r}^*, T^*) = (0.592 [1.034 \text{ gcm}^{-3}], 0.95 [135 \text{ K}])$ ; for xenon at the state point  $(\mathbf{r}^*, T^*) = (0.6 [2.222 \text{ gcm}^{-3}], 0.9 [252.9 \text{ K}])$ . These points were chosen because they are representative of the liquid phase being approximately midway between the triple point and the critical point (for both argon and xenon). The

number of atoms in our systems was  $N = 500$ , and the size of our simulation cell,  $L$ , was 9.453 (reduced units) for argon and 9.410 (reduced units) for xenon. The three-body terms were truncated at  $0.25L$ , whereas the two-body terms were truncated at  $0.5L$ . These cut-off distances further ensured that the total non-equilibrium pair distribution function was constant (i.e., equal to unity) over the range of  $r$  where long-range corrections are applied.

Table 4.1 Pressure, energy and shear viscosity at different strain rates for argon.

$\dot{\mathbf{g}}^*$	2-body potential without 3-body potential			2-body potential with 3-body potential		
	$P^*$	$E_{conf}^*$	$\mathbf{h}^*$	$P^*$	$E_{conf}^*$	$\mathbf{h}^*$
0.0	-0.103(2)	-3.682(2)		0.017(2)	-3.557(1)	
0.078	-0.105(1)	-3.683(1)	0.72(2)	0.019(2)	-3.555(1)	0.72(3)
0.1755	-0.108(1)	-3.679(1)	0.754(5)	0.020(2)	-3.554(1)	0.742(6)
0.24	-0.102(2)	-3.683(2)	0.747(6)	0.022(1)	-3.552(1)	0.732(6)
0.312	-0.103(2)	-3.677(1)	0.753(2)	0.024(2)	-3.551(1)	0.733(5)
0.4	-0.099(1)	-3.673(1)	0.747(1)	0.031(2)	-3.550(1)	0.725(1)
0.5	-0.092(4)	-3.667(3)	0.746(6)	0.034(3)	-3.541(1)	0.725(6)
0.702	-0.079(2)	-3.656(1)	0.727(2)	0.054(1)	-3.529(1)	0.719(1)
0.9555	-0.050(1)	-3.631(2)	0.715(1)	0.084(2)	-3.511(1)	0.703(2)
1.248	0.002(1)	-3.595(1)	0.699(1)	0.135(1)	-3.480(1)	0.689(1)
1.5795	0.076(1)	-3.558(1)	0.677(1)	0.214(1)	-3.443(1)	0.668(1)
1.95	0.179(2)	-3.506(1)	0.653(1)	0.312(2)	-3.396(1)	0.644(1)

Table 4.2 Pressure, energy and shear viscosity at different strain rates for xenon.

$\dot{\mathbf{g}}^*$	2-body potential without 3-body potential			2-body potential with 3-body potential		
	$P^*$	$E_{conf}^*$	$\mathbf{h}^*$	$P^*$	$E_{conf}^*$	$\mathbf{h}^*$
0.0	-0.161(1)	-3.696(1)		0.012(4)	-3.512(2)	
0.2	-0.156(6)	-3.672(4)	0.77(1)	0.0150(1)	-3.509(1)	0.76(1)
0.4	-0.152(5)	-3.688(2)	0.772(3)	0.0243(9)	-3.5022(4)	0.765(2)
0.6	-0.138(2)	-3.683(5)	0.758(4)	0.0387(2)	-3.4938(1)	0.749(1)
0.8	-0.1187(8)	-3.660(1)	0.753(4)	0.065(1)	-3.4795(6)	0.739(1)
1	-0.088(6)	-3.6354(7)	0.7438(7)	0.092(2)	-3.4628(8)	0.7263(8)
1.2	-0.0527(1)	-3.611(2)	0.733(2)	0.132(3)	-3.443(3)	0.716(2)
1.4	-0.0073(9)	-3.5875(5)	0.717(1)	0.184(4)	-3.4211(1)	0.706(1)
1.6	0.046(3)	-3.5577(4)	0.7021(3)	0.237(1)	-3.395(1)	0.6892(7)
1.8	0.1073(6)	-3.5304(6)	0.6882(9)	0.298(1)	-3.3689(3)	0.6789(8)

The uncertainties in the time averages for the energy, pressure and viscosity, reported in Tables 4.1 and 4.2, represent the standard errors of the averages over 5 independent non-equilibrium trajectories for argon and over 2 independent non-equilibrium trajectories for xenon. The data include calculations with the two-body potential alone and a combined two-body + AT potential. We confirmed that the two and three-body energies and pressures at equilibrium were correct by comparing them with independent calculations of these quantities obtained by Monte Carlo simulations [All87].

These results, and various attempts to fit the simulation data, are illustrated in Figures 4.4 - 4.10. In Tables 4.3 and 4.4 the coefficients of the fits are presented, as well as their respective errors. Additionally, the coefficients of both fitted equations and the absolute average deviations (AAD) [Sad95] are given. The AAD is a measure of the overall accuracy of the agreement between the fits and the simulation data and is defined as:

$$\text{AAD}(\%) = 100 \times \sum_{i=1}^s \frac{1}{s} \left| \frac{f^{\text{simul.}}(\dot{\mathbf{g}}_i) - f^{\text{fit}}(\dot{\mathbf{g}}_i)}{f^{\text{simul.}}(\dot{\mathbf{g}}_i)} \right| \quad (4.4)$$

where  $s$  is the number of data points,  $f^{\text{simul.}}(\dot{\mathbf{g}}_i)$  is the simulation value of the quantity considered (pressure, energy or viscosity) as a function of  $\dot{\mathbf{g}}_i$  and  $f^{\text{fit}}(\dot{\mathbf{g}}_i)$  is the value taken from the fitting curve.

Table 4.3 Coefficients of the fits and relative errors for argon.

	$a^*$	$b^*$	AAD %
$P = a + b\dot{g}^{3/2}$	0.0032(6)	0.1039(5)	26.72
$P = a + b\dot{g}^2$	0.0164(6)	0.0781(4)	3.97
$E = a + b\dot{g}^{3/2}$	-3.5607(4)	0.0592(3)	0.08
$E = a + b\dot{g}^2$	-3.5554(4)	0.0430(2)	0.09
$h = a + b\dot{g}^{1/2}$	0.800(2)	-0.105(2)	1.60
$h = a + b\dot{g}$	0.752(1)	-0.0535(8)	0.74
$h = a + b\dot{g}^{3/2}$	0.7360(8)	-0.0339(5)	0.45
$h = a + b\dot{g}^2$	0.7279(7)	-0.0229(3)	0.69

Table 4.4 Coefficients of the fits and relative errors for xenon.

	$a^*$	$b^*$	AAD %
$P = a + b\dot{g}^{3/2}$	0.0027(1)	0.1054(3)	16.04
$P = a + b\dot{g}^2$	0.0108(1)	0.0868(3)	3.49
$E = a + b\dot{g}^{3/2}$	-3.5224(1)	0.0616(1)	0.08
$E = a + b\dot{g}^2$	-3.5094(1)	0.0447(1)	0.04
$h = a + b\dot{g}^{1/2}$	0.849(2)	-0.125(2)	0.86
$h = a + b\dot{g}$	0.7863(2)	-0.0598(8)	0.38
$h = a + b\dot{g}^{3/2}$	0.7654(8)	-0.0367(5)	0.31
$h = a + b\dot{g}^2$	0.7549(7)	-0.0247(3)	0.57

Mode-coupling theory [Kaw73] predicts that the pressure of a fluid under shear has a linear dependence with  $\dot{g}^{3/2}$ . To test this prediction, we plot the total pressure of the fluid against  $\dot{g}^{3/2}$  in Figure 4.4(a) for argon and in Figure 4.5(a) for xenon. If the pressure were a linear function of  $\dot{g}^{3/2}$  one would expect random statistical fluctuations in the data points about the linear fit. However, a careful analysis of the data suggests a systematic deviation from the expected  $\dot{g}^{3/2}$  linear behaviour.

In Figure 4.4(b) for argon and in Figure 4.5(b) for xenon the total pressure is presented as a function of  $\dot{g}^2$ . We find that the pressure is more closely represented by an analytic  $\dot{g}^2$  dependence.

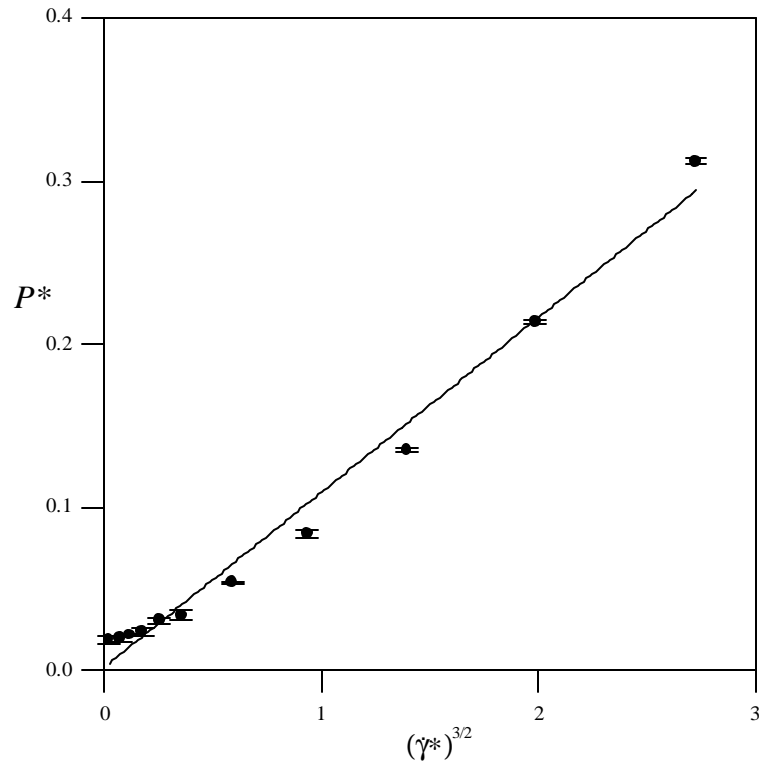


Figure 4.4a Total pressure of argon as function of  $\dot{g}^{3/2}$  using 2-body + 3-body potentials.

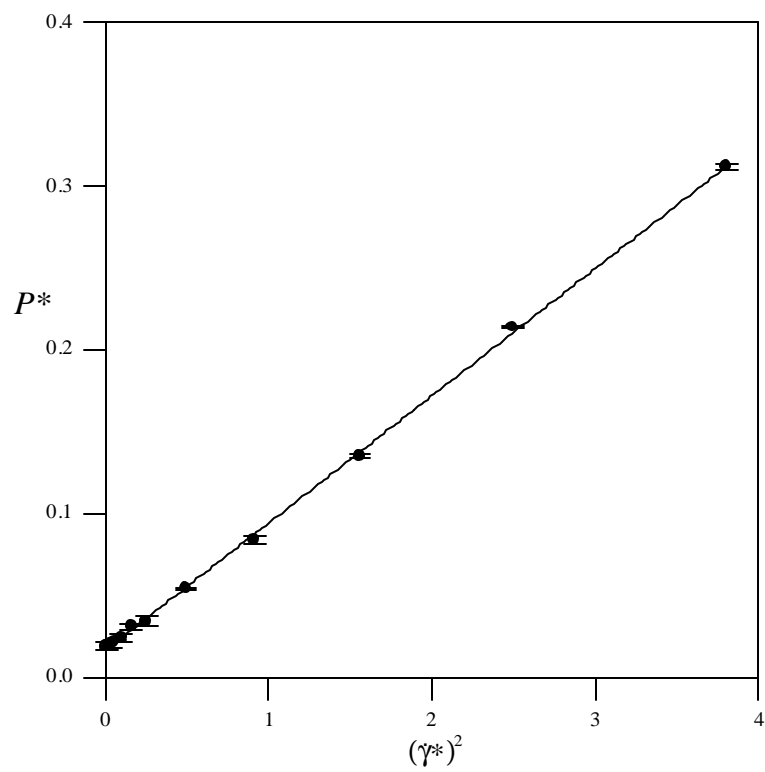


Figure 4.4b Total pressure of argon as function of  $\dot{g}^2$  using 2-body + 3-body potentials.

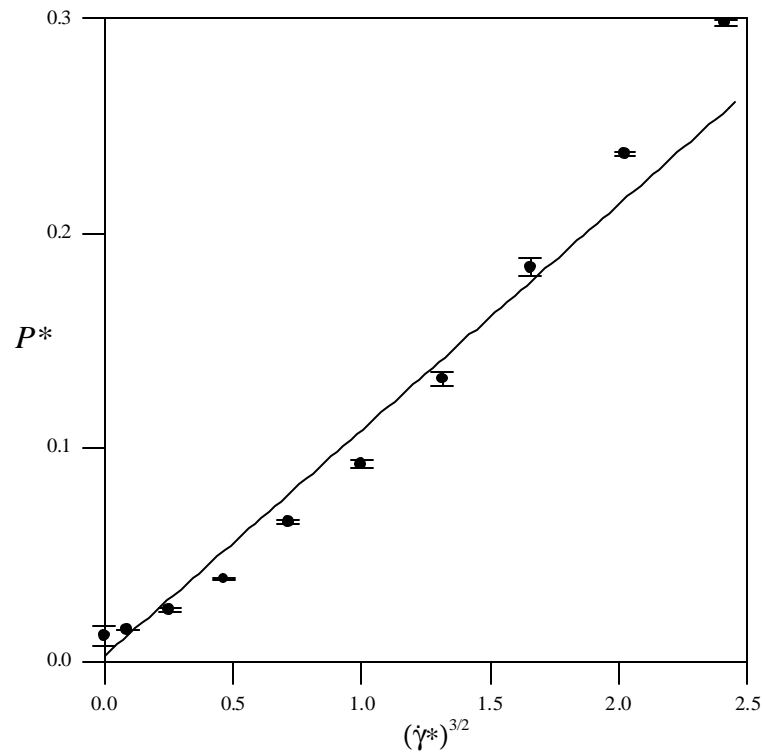


Figure 4.5a Total pressure of xenon as function of  $\dot{g}^{3/2}$  using 2-body + 3-body potentials.

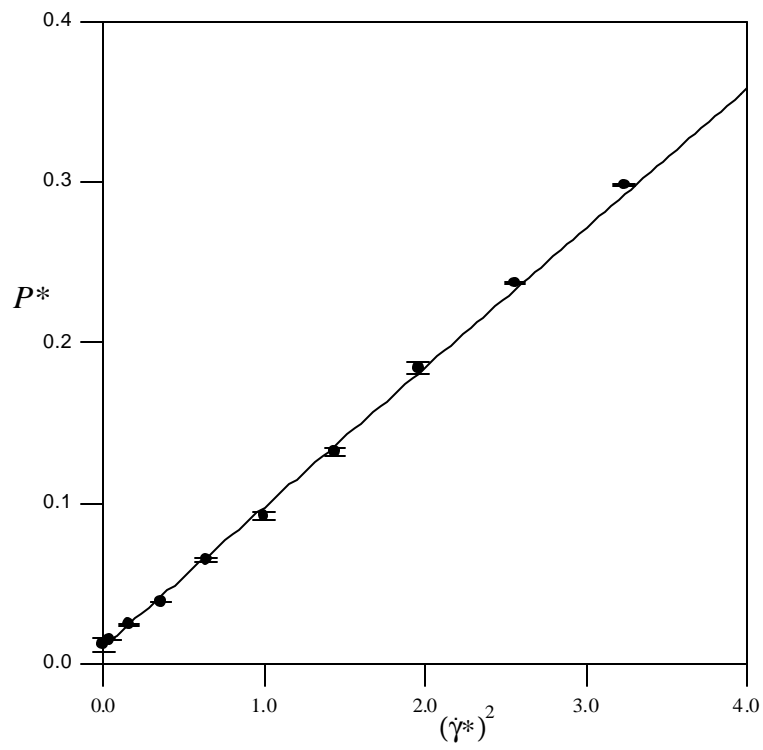


Figure 4.5b Total pressure of xenon as function of  $\dot{g}^2$  using 2-body + 3-body potentials.

For argon at equilibrium, a pressure of approximately 1 MPa is predicted compared with an experimental value of 4 MPa [Var75]. The main contribution to the overall pressure comes from the kinetic component and two-body interactions which are of similar magnitude but of opposite sign. This means that small statistical fluctuations in the two-body contribution can greatly affect both the magnitude and sign of the total pressure. Unfortunately, a similar comparison for the xenon pressure at equilibrium is not possible because to the best of our knowledge, experimental data for the state point we used are not available.

To determine whether the  $\dot{\mathbf{g}}^2$  dependence is due to the addition of three-body interactions, we plot the two-body and full two- plus three-body contributions to the total pressure separately in Figures 4.6a and 4.6b (for argon and xenon respectively). The results for the two-body pressures are obtained from simulations involving only the two-body BFW potential interactions, without the three-body terms. It is evident that the  $\dot{\mathbf{g}}^2$  dependence is caused by two-body interactions. The three-body contributions serve only to shift the pressures higher by approximately 0.1 for argon and 0.18 for xenon. Although it could be reasonably expected that the three-body contribution to the total pressure might depend on strain rate, our simulation results suggest that any dependence is very weak for the strain rates covered.

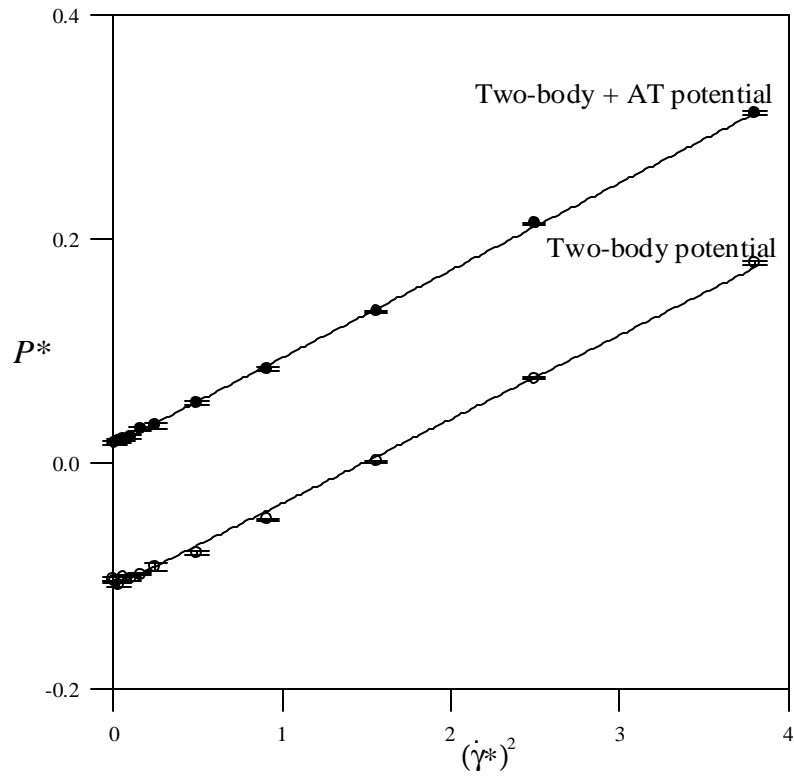


Figure 4.6a Total pressure of argon using only two-body potential ( $\circ$ ); total pressure using 2-body + 3-body potentials ( $\bullet$ ).

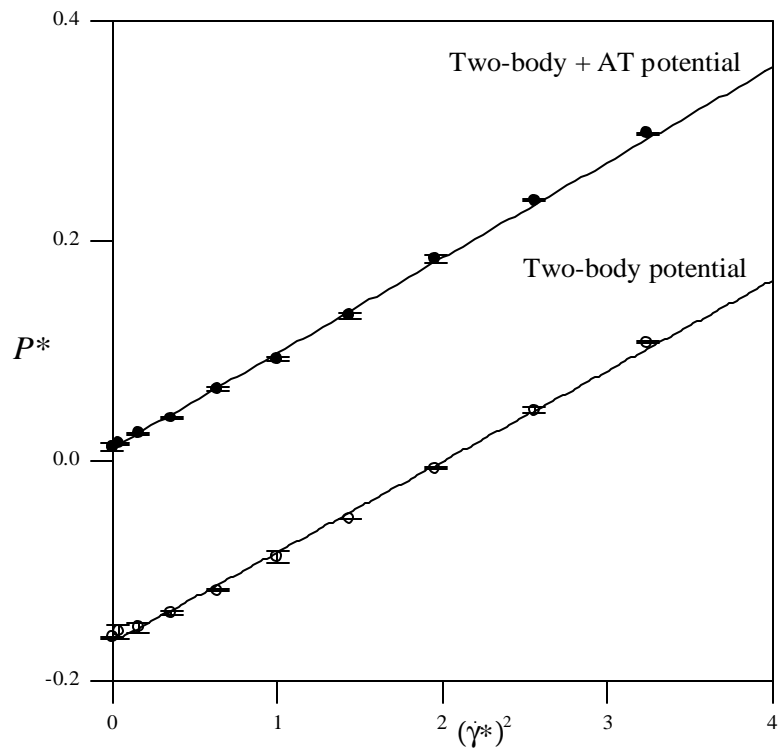


Figure 4.6b Total pressure of xenon using only two-body potential ( $\circ$ ); total pressure using 2-body + 3-body potentials ( $\bullet$ ).

The configurational energy per particle is presented as a function of  $\dot{\mathbf{g}}^{3/2}$  and  $\dot{\mathbf{g}}^2$  in Figures 4.7 (a-b) for argon and Figures 4.8 (a-b) for xenon. The  $E$  vs.  $\dot{\mathbf{g}}^{3/2}$  plot does show a weak systematic departure from linearity. For argon the fits in  $\dot{\mathbf{g}}^{3/2}$  and  $\dot{\mathbf{g}}^2$  are similar in accuracy, but for xenon the fit in  $\dot{\mathbf{g}}^2$  is much better. The coefficients of the fits, along with the absolute average deviation are presented in Table 4.3 for argon and in Table 4.4 for xenon.

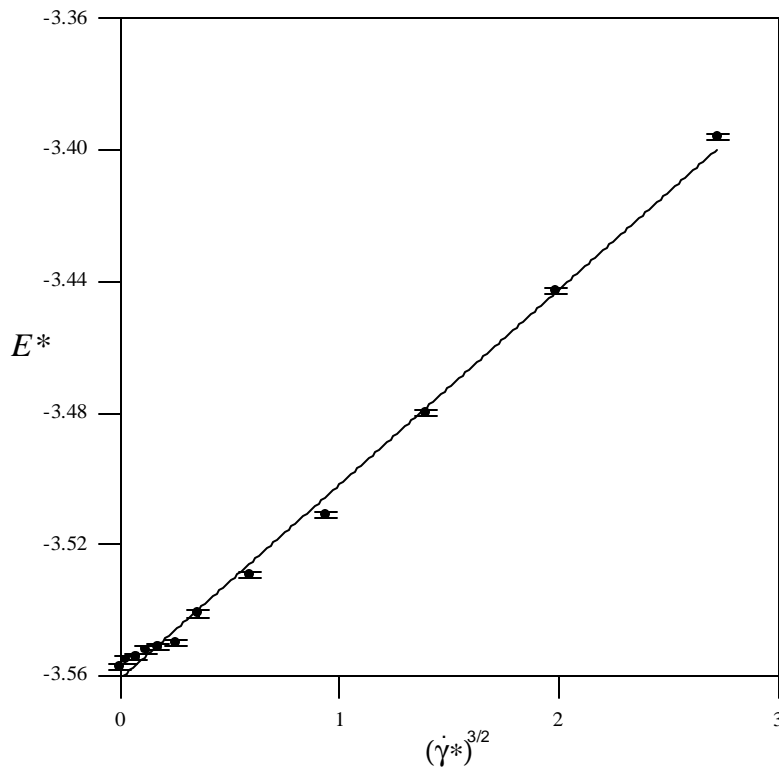


Figure 4.7a The 2-body + 3-body potential energy of argon as function of  $\dot{\mathbf{g}}^{3/2}$ .

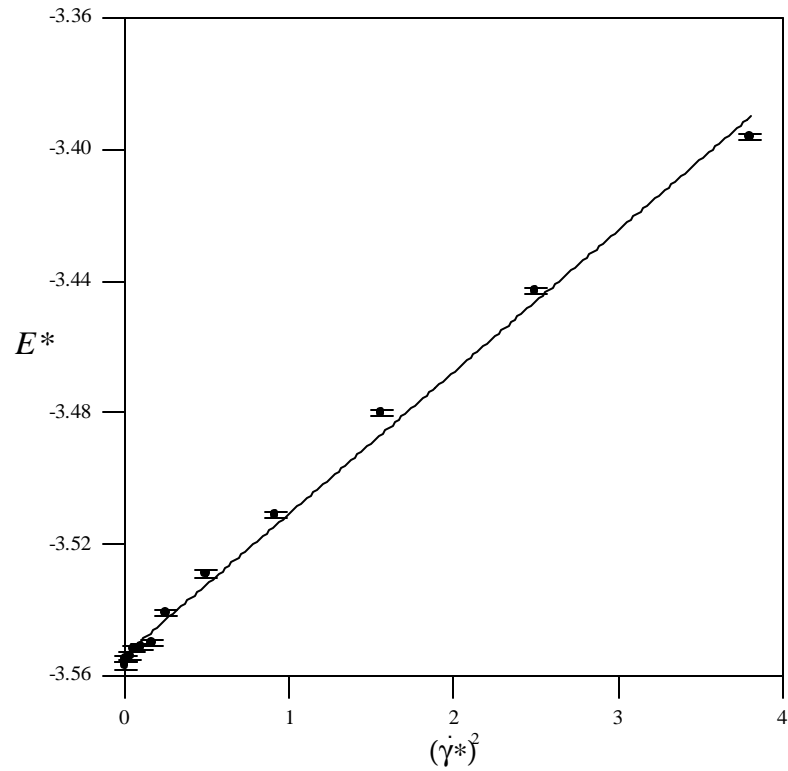


Figure 4.7b The 2-body + 3-body potential energy of argon as function of  $\dot{g}^2$ .

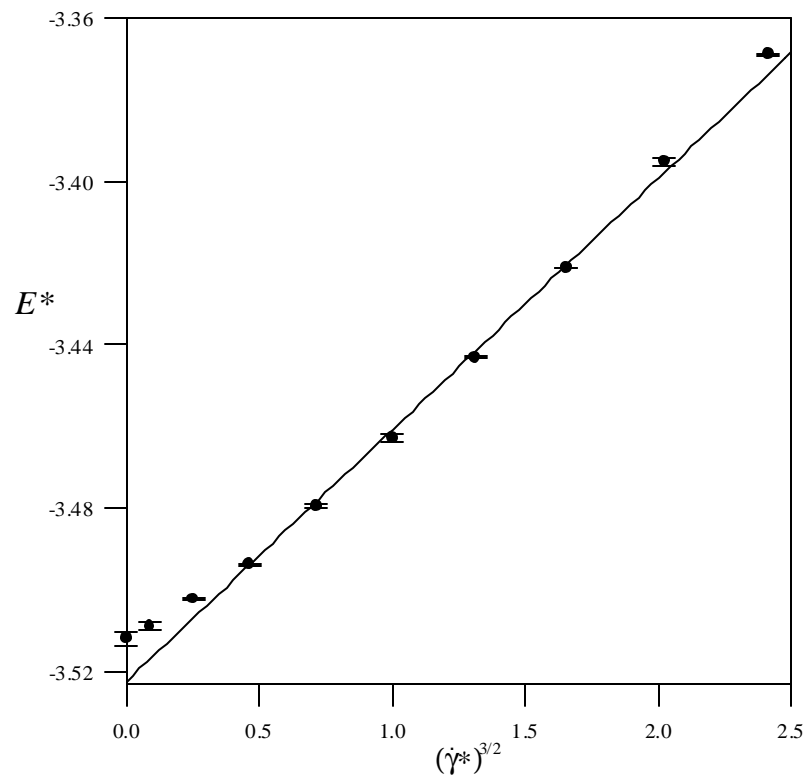


Figure 4.8a The 2-body + 3-body potential energy of xenon as function of  $\dot{g}^{3/2}$ .

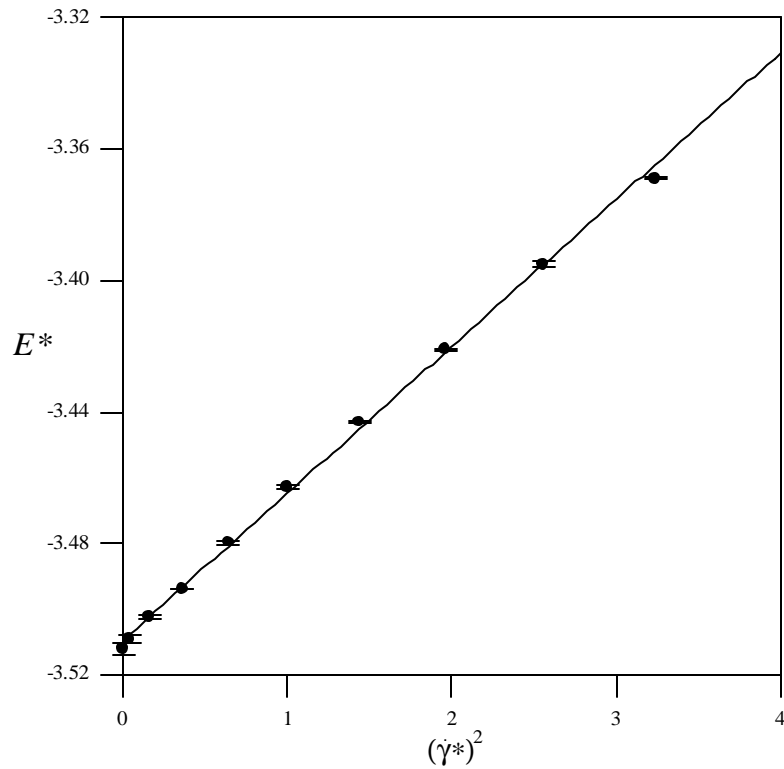


Figure 4.8b The 2-body + 3-body potential energy of xenon as function of  $\dot{\gamma}^2$ .

The shear viscosity of the fluid, calculated as  $\mathbf{h} = \frac{-\langle P_{xy} + P_{yx} \rangle}{2\dot{\mathbf{g}}}$ , is plotted against  $\dot{\mathbf{g}}$  in Figure 4.9 for argon and in Figure 4.10 for xenon. The viscosity is not a simple function of  $\dot{\mathbf{g}}^{1/2}$ , which is consistent with the conclusion reached by Travis et al [Tra98]. The statistical errors in our viscosity calculations are not sufficiently small to unambiguously determine the functional form of the viscosity profile. Any fit of  $\mathbf{h}$  vs.  $\dot{\mathbf{g}}^n$  is reasonable, where  $1/2 \leq n \leq 2$ . For argon however, when the data is extrapolated to zero strain-rate, the values of the equilibrium viscosity predicted by the  $\dot{\mathbf{g}}$ ,  $\dot{\mathbf{g}}^{3/2}$  and  $\dot{\mathbf{g}}^2$  fits  $[(757 \pm 1) \times 10^7, (741 \pm 1) \times 10^7, (733 \pm 1) \times 10^7 \text{ Nsm}^{-2}]$ , respectively] are in good agreement with the experimental value of  $740.2 \times 10^7 \text{ Nsm}^{-2}$  [Var75]. The  $\dot{\mathbf{g}}^{1/2}$  fit actually gives the worst agreement  $[(805 \pm 3) \times 10^7 \text{ Nsm}^{-2}]$  with the experiment.

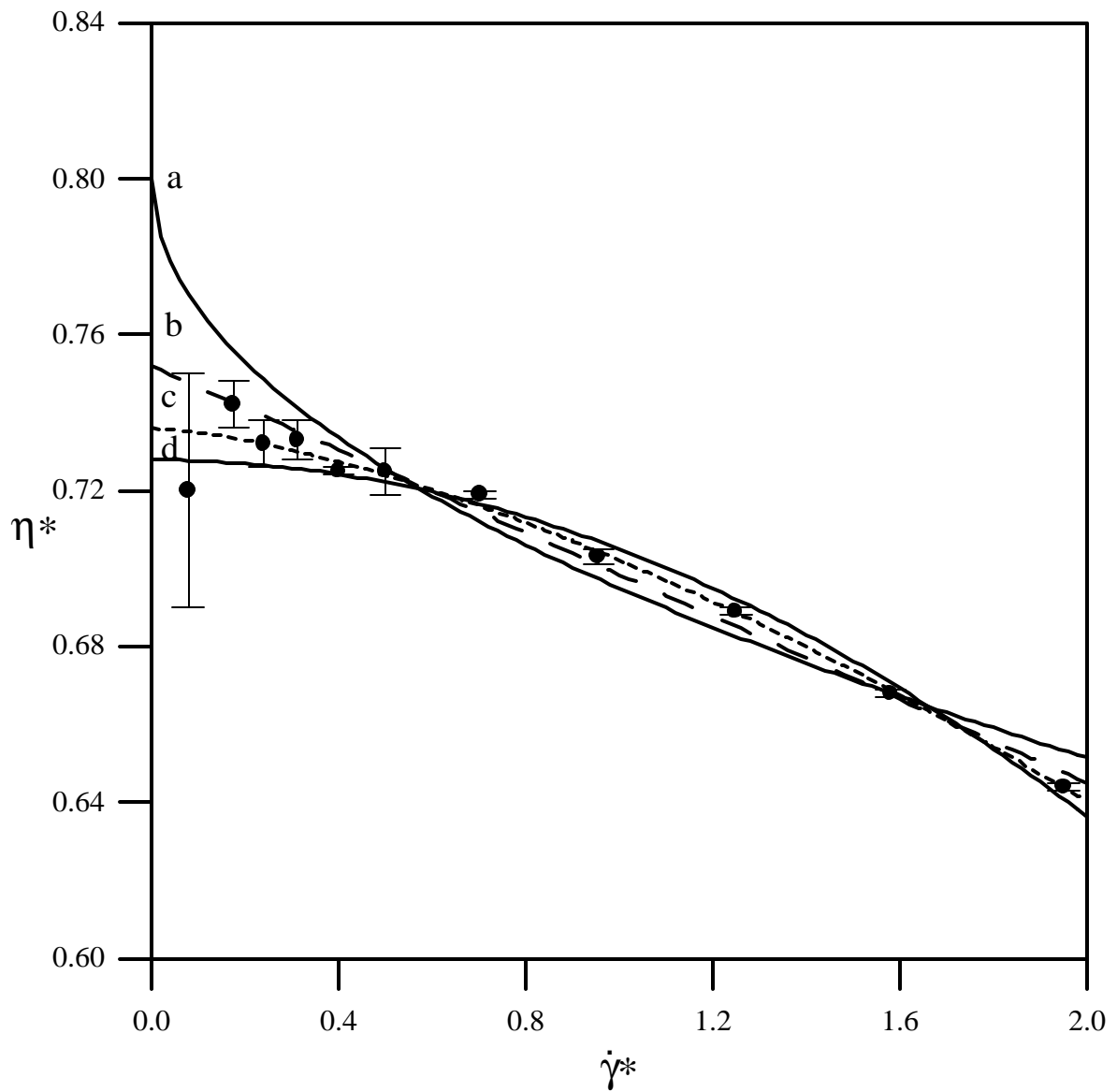


Figure 4.9 Viscosity of argon as function of the strain rate. The lines illustrate different fits with strain rate dependence to the power of (a) 1/2, (b) 1, (c) 3/2 and (d) 2. The parameters of these fits are in Table 4.3.

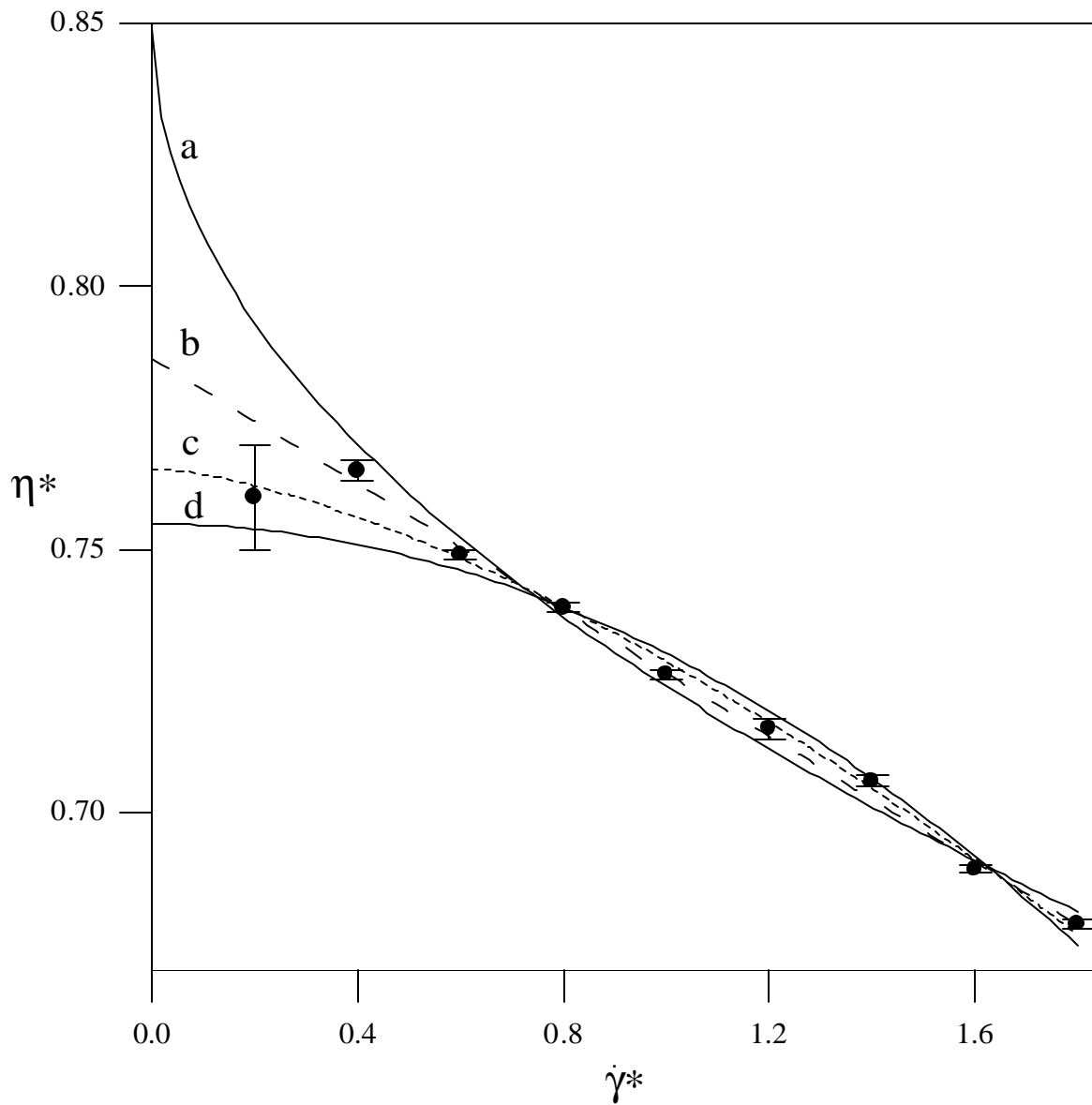


Figure 4.10 Viscosity of xenon as function of the strain rate. The lines illustrate different fits with strain rate dependence to the power of (a) 1/2, (b) 1, (c) 3/2 and (d) 2. The parameters of these fits are in Table 4.4.

Our results differ to those of Lee and Cummings [Lee93, Lee94], who observed the standard  $\dot{g}^{3/2}$  dependence of the pressure with strain rate. Lee and Cummings used a system size of 108 argon atoms for both the BFW and BFW + AT calculations. Quantitative error estimates were not reported with their data. Normally, large errors in pressure can be expected for simulations involving such a small number of atoms, which can hinder the correct identification of the strain-rate dependency of pressure. We repeated their simulations for 108 argon atoms at the same state point with only the two-body BFW potential, and present the results for the pressure and energy dependence on strain rate in Figures 4.11 and Figure 4.12, respectively. Our simulations were performed by time averaging over a total of  $2 \times 10^6$  time-steps, and our statistics are thus more reliable. We do not include long-range corrections to this set of data, which would only add a constant term to shift the pressure and energy profiles. It does not change the shape, which is what we are interested in. Once again our results confirm the  $\dot{g}^2$  dependence of both pressure and energy.

We make the observation that a system size of 108 particles is actually too small to account fully for all the possible three-body interactions, and for this reason we performed the 108 atom simulations only with the two-body BFW potential. The cut-off value for the three-body potential should not exceed one quarter of the length of the simulation cell, for geometrical constraints imposed by the three-body interactions (see Appendix 2). In their system, Lee and Cummings used a cell length,  $L$ , of 5.67 (reduced units). Their cut off radius was  $0.5L = 2.835$  (reduced units), which is too large for their small system size. It is primarily for such reasons that we choose to study a larger system size of 500 atoms.

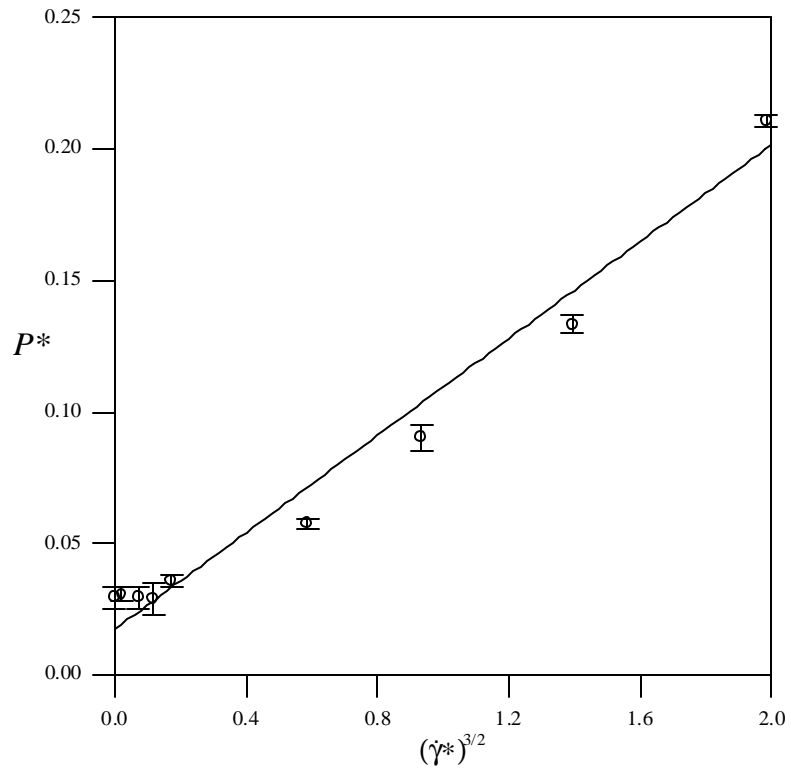


Figure 4.11a Total pressure of argon as function of  $\dot{g}^{3/2}$  for 108-atom system.

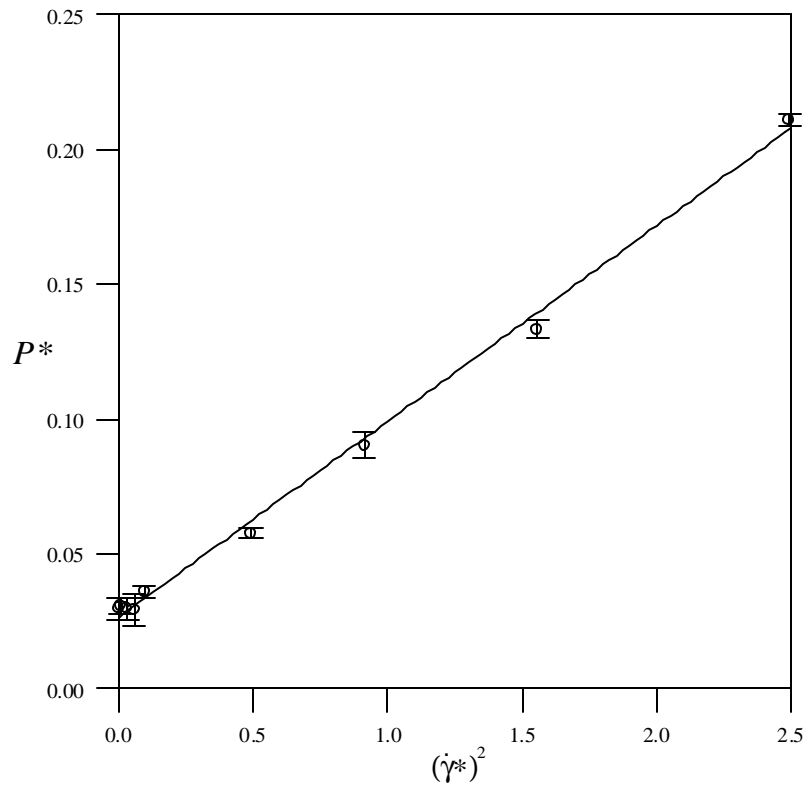


Figure 4.11b Total pressure of argon as function of  $\dot{g}^2$  for 108-atom system.

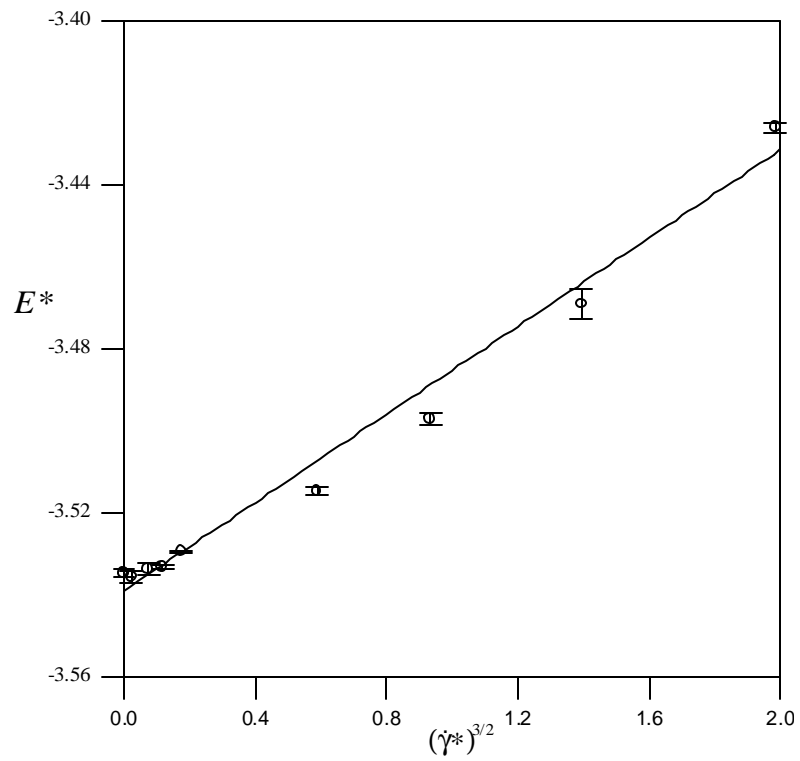


Figure 4.12a Potential energy of argon as function of  $g^{3/2}$  for 108-atom system.

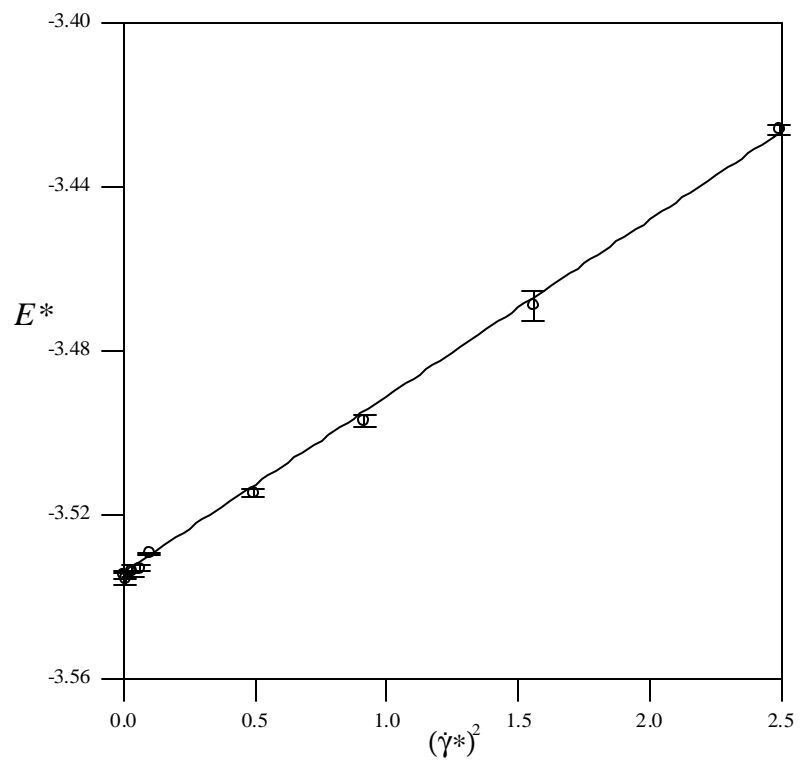


Figure 4.12b Potential energy of argon as function of  $g^2$  for 108-atom system.

The pressure tensor of the fluid was calculated by the standard Irving-Kirkwood expression [Irv50], modified to include 3-body contributions (see Appendix 2):

$$\langle \mathbf{P} \rangle = \frac{1}{V} \left\langle \sum_{i=1}^N \frac{\mathbf{p}_i \mathbf{p}_i}{m} + \sum_{i=1}^{N-1} \sum_{j>i}^N \frac{\mathbf{r}_{ij} \mathbf{F}_{ij}^{2b}}{m} + \sum_{i=1}^{N-2} \sum_{j>i}^{N-1} \sum_{k>j}^N \left[ \mathbf{r}_{ij} \mathbf{F}_{(ij)k}^{3b} + \mathbf{r}_{ik} \mathbf{F}_{(ik)j}^{3b} + \mathbf{r}_{jk} \mathbf{F}_{(jk)i}^{3b} \right] \right\rangle \quad (4.5)$$

where  $\mathbf{p}_i$  is the peculiar momentum of atom  $i$ .  $\mathbf{F}_{ij}^{2b}$  is the two-body force between atom  $i$

and  $j$ , and terms involving  $\mathbf{F}_{(ab)k}^{3b} = \frac{\partial u_{abk}^{3b}}{\partial \mathbf{r}_{ab}}$  are the corresponding three-body

contributions to the total force. The definition of the pressure we used is one third of the of the trace of the pressure tensor (see also Chapter 2):

$$P = \frac{1}{3} \text{Tr} \langle \mathbf{P} \rangle = \frac{1}{3V} \langle P_{xx} + P_{yy} + P_{zz} \rangle \quad (4.6)$$

To check that there was no error in the evaluation of Eq. (4.5), we calculated the configurational part of the pressure by another independent method, namely by integrating over the *total* non-equilibrium pair distribution function. This method will allow us to calculate the two-body potential contribution to the pressure. The three-body potential contribution to the pressure was checked by the relationship  $P^{3b} = 3E/V$  ([Bar71a], see also Appendix 2). Since we keep the temperature and density constant, the kinetic contribution to the pressure is constant and given simply by  $P^{Kin} = \mathbf{r}T$  (see Eq. (2.65)).

During the simulation we calculated the pair radial distribution function,  $g(r)$ , via Eq. (2.93). Therefore, we were able to calculate the two-body potential pressure in two ways: directly using Eqs. (4.5) and (4.6) (2-body potential part) and *indirectly* using  $g(r)$  with Eq. (2.101).

Following the same procedure, we calculated the two-body potential energy directly using the expression:

$$E = \frac{1}{N} \left\langle \sum_{i=1}^{N-1} \sum_{j>i}^N u_{ij}^{2b} \right\rangle \quad (4.7)$$

and *indirectly* using Eq. (2.102). Furthermore, we calculated the quantity  $\mathbf{n}(r)$  using Eq. (2.96) during the same simulation to calculate the shear viscosity *indirectly* via Eq. (2.103).

In Table 4.5 we show the two-body components of the pressure, energy and viscosity (for argon) calculated by Eqs. (2.101), (2.102) and (2.103) alongside of the direct values for different strain rates  $\dot{\mathbf{g}}$ . For every value of  $\dot{\mathbf{g}}$ , the quantities were calculated over a single trajectory of 50000 time-steps. Very good agreement (up to the fourth decimal place) is found between the direct calculations and those involving  $g(r, \dot{\mathbf{g}})$  and  $\mathbf{n}(r, \dot{\mathbf{g}})$ . This agreement suggests that the observed dependencies of the pressure, energy and viscosity with strain rate are not a result of an error in the direct calculations of these properties.

Table 4.5 Two-body contributions of the pressure, energy and viscosity of argon.

$\dot{\mathbf{g}}^*$	$P_{2body}^*$ (simulation)	$P_{2body}^*$ ( $g(r, \dot{\mathbf{g}})$ )	$E_{2body}^*$ (simulation)	$E_{2body}^*$ ( $g(r, \dot{\mathbf{g}})$ )	$\mathbf{h}_{2body}^*$ (simulation)	$\mathbf{h}_{2body}^*$ ( $\mathbf{n}(r, \dot{\mathbf{g}})$ )
0.0	-0.7136	-0.7136	-3.6384	-3.6382	-	-
0.702	-0.6720	-0.6720	-3.6118	-3.6118	0.6017	0.6016
0.9555	-0.6382	-0.6383	-3.5941	-3.5941	0.5899	0.5899
1.248	-0.5869	-0.5870	-3.5547	-3.5547	0.5837	0.5837
1.549	-0.5018	-0.5019	-3.5165	-3.5165	0.5671	0.5671
1.95	-0.4045	-0.4046	-3.4738	-3.4738	0.5436	0.5436

In Figure 4.13 we display  $g(r, \dot{\mathbf{g}})$  and  $\mathbf{n}(r, \dot{\mathbf{g}})$  for the fluid shearing with a strain rate of  $\dot{\mathbf{g}}^* = 1.95$ . Additionally, we include  $g(r, \dot{\mathbf{g}})$  at equilibrium ( $\dot{\mathbf{g}}^* = 0$ ) for comparison purposes. The difference between  $g(r, \dot{\mathbf{g}})$  for  $\dot{\mathbf{g}}^* = 0$  and  $\dot{\mathbf{g}}^* = 1.95$  reflects the change

in the fluid structure with imposed strain rate, which is to be expected. It is well known that  $g(\mathbf{r}, \dot{\mathbf{g}})$  (Eq. (2.94)) is no longer spherically symmetric at large values of  $\dot{\mathbf{g}}$  [Eva90], but becomes distorted at an angle of 45 degrees to the fluid velocity streamlines.

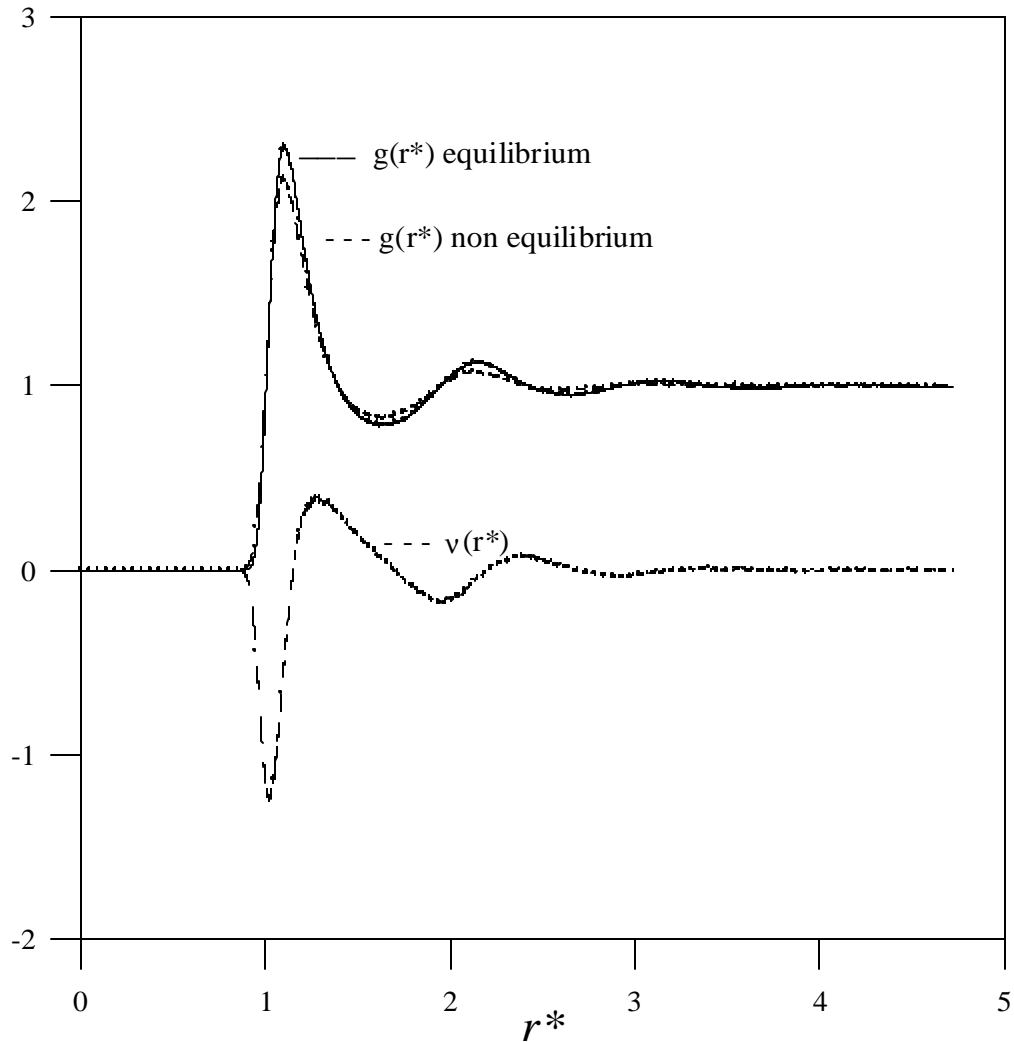


Figure 4.13  $g(r, \dot{\mathbf{g}})$  and  $\mathbf{n}(r, \dot{\mathbf{g}})$  for the argon fluid shearing at the highest strain rate used ( $\dot{\mathbf{g}}^* = 1.95$ ).  $g(r, \dot{\mathbf{g}})$  at equilibrium ( $\dot{\mathbf{g}}^* = 0$ ) is also reported.

There is an additional check we can perform to ensure that the SLLOD algorithm was correctly implemented, and that the pressure tensor was correctly calculated. For thermostatted planar Couette flow, the rate of energy dissipation may be expressed as:

$$\dot{H}(t) = -VP_{xy}\dot{\mathbf{g}} - \mathbf{a} \sum_{i=1}^N \frac{\mathbf{p}_i \cdot \mathbf{p}_i}{m} \quad (4.8)$$

where  $\dot{H}(t)$  is the time derivative of the total internal energy. For the algorithm to be working correctly, and for the shear stress to be correctly calculated, the right-hand-side (RHS) of Eq. (4.8) must equal the left-hand-side (LHS) for all  $t$ . This was indeed found to be the case in all our simulations, as seen in Figure 4.14.

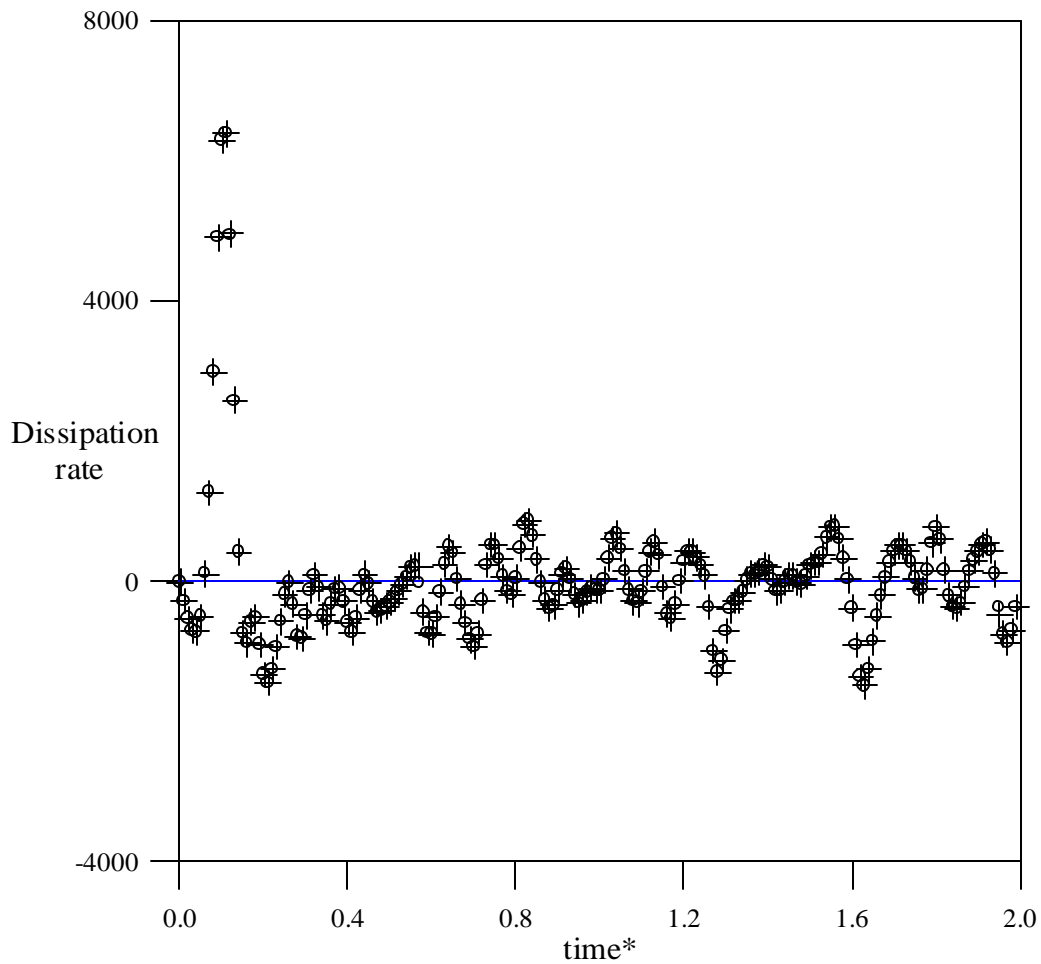


Figure 4.14 Comparison of RHS of Eq. (4.8) (+), and LHS (o). Note that at  $t^*=0$  the strain rate is imposed, and the fluid takes time to relax to a non-equilibrium steady state.

Figure 4.14 displays the results for a simulation where the shear stress is applied at  $t^*=0$ , from an equilibrium state. The high peak close to  $t^*=0$  reveals that an initial amount of energy, provided by the shearing, goes to change the internal structure of the fluid, from an equilibrium state to a non-equilibrium one. Referring to Figure 4.13, this amount of energy is utilized to distort the equilibrium  $g(r)$ . After this initial transition, the system reaches a steady state.

Additionally, we checked that the hydrostatic pressure calculation was correct by calculating the dissipation for a fluid undergoing planar elongation. The dissipation is related to differences in the diagonal elements of the pressure tensor, and the dissipation rate is given as:

$$\dot{H}(t) = -V\dot{\mathbf{e}}[P_{xx} - P_{yy}] - \mathbf{a} \sum_{i=1}^N \frac{\mathbf{p}_i \cdot \mathbf{p}_i}{m} \quad (4.9)$$

Here  $\dot{\mathbf{e}}$  is the elongation strain rate, and the fluid expands in the  $x$ -direction, whilst simultaneously contracting in the  $y$ -direction. Details of the simulation algorithm for planar elongation can be found elsewhere [Tod97, Tod99]. Our simulations confirmed the equivalence of the RHS and LHS of Eq. (4.9).

Previous work [Ryc88] that had attempted to show the analytic dependence of the viscosity on  $\dot{\mathbf{g}}$  was criticized for the relatively high rates of strain used [Tra98]. Large strain rates can induce unwanted string phases, i.e., highly ordered solid-like configurations. These string phases arise for high Reynolds number flows [Erp84], where the assumption of a linear streaming velocity profile is questionable. The linear profile is imposed upon the flow via the SLLOD equations of motion. For a freely shearing system with Lees-Edwards periodic boundary conditions, high Reynolds number flows should exhibit an S-shaped kink in the streaming velocity profile. If the assumed (linear) and actual streaming velocities are not the same, the thermostat

interprets this deviation as heat, and applies an additional force to the equations of motion for the momenta (see Eq. (2.79)). It is this additional force appearing in the term involving  $\mathbf{a}$  that serves to stabilize the linear velocity profile and enhance the ordering of the fluid by reducing the rate of entropy production. Once the fluid's ordering is enhanced, its viscosity and pressure are reduced dramatically from their true values, which can lead to incorrect dependencies on  $\dot{\mathbf{g}}$ .

In Figure 4.15 we project a 3-dimensional snapshot of the argon fluid onto a 2-dimensional surface in the  $x$ - $y$  plane. The fluid was sheared at the highest value of  $\dot{\mathbf{g}}$  which we simulated,  $\dot{\mathbf{g}}^* = 1.95$ .

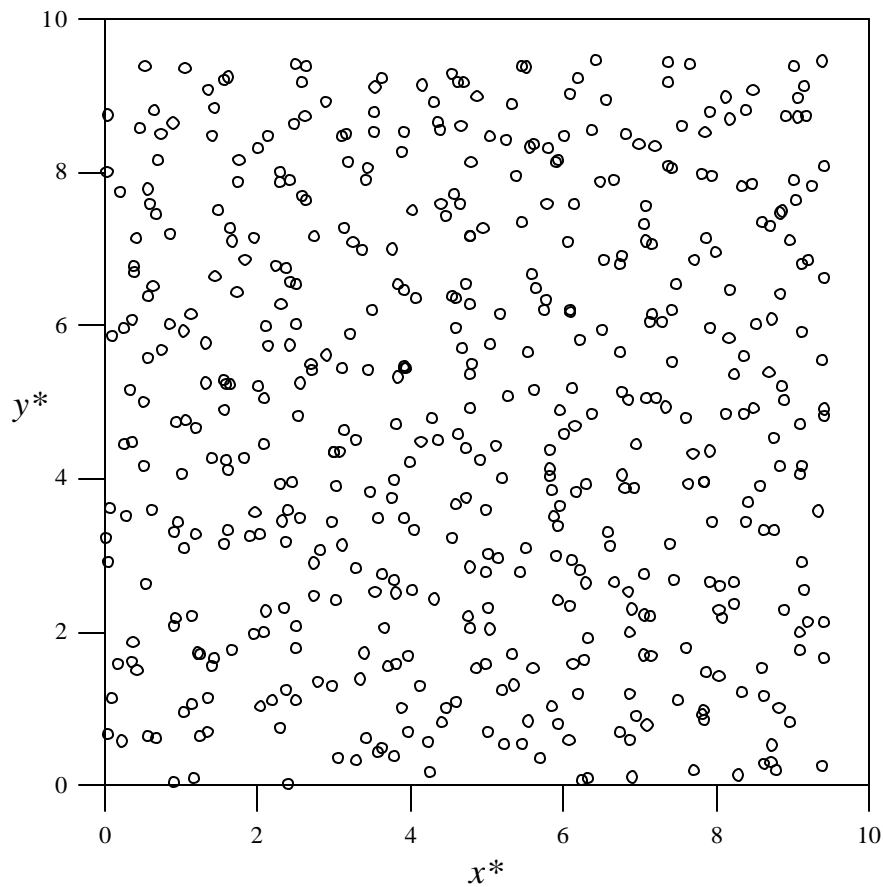


Figure 4.15 Two-dimensional projection onto the  $x$ - $y$  plane of a three-dimensional snapshot of the argon fluid, shearing at the highest strain rate used ( $\dot{\mathbf{g}}^* = 1.95$ ).

There is no obvious enhancement in the structure of the fluid. For our system, strings were only noticeable at very high values of  $\dot{g}$ , typically  $\dot{g}^* > 5$ . This is in contrast to work by Evans et al. [Eva92], who found evidence of strings for values of  $\dot{g}^*$  as low as  $\sim 2$ . However, their simulations were performed on a Weeks-Chandler-Anderson (WCA) fluid [Wee71]. Our simulations have been performed on BFW fluids, both with and without the additional three-body term, where the range over which fluid atoms interact is significantly greater than for WCA fluids. In Figure 4.16 we show a full 3-dimensional snapshot of the fluid sheared at  $\dot{g}^* = 11$ , where now the appearance of strings is very pronounced. If strings were formed in our simulations, the anticipated side-effect should be to dramatically reduce the values of the viscosity and hydrostatic pressure at higher strain rates. Our data clearly does not support this.

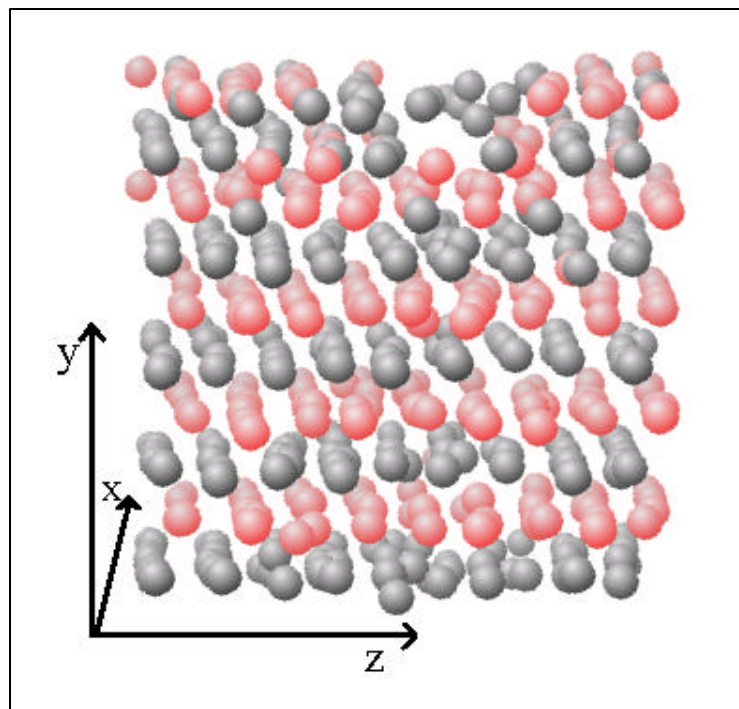


Figure 4.16 Full three-dimensional snapshot of the argon fluid, shearing at high value of  $\dot{g}^* = 11$ .

Finally, we checked the dependence of the pressure, energy and viscosity profiles on the size of the cut-off potential radius used. While the results presented here for argon were performed with a two-body cut-off radius of  $r_{cut-off}^{2b} = 0.5L = 4.726$  (reduced units), we also performed simulations at a smaller cut-off of  $r_{cut-off}^{2b} = 2.28$  (reduced units) for an argon system of 500 atoms. The shapes of these profiles remained unchanged.

### 4.3 Relationship between two-body and three-body potentials from NEMD simulation

It is of interest to determine the effect of different strain rates on the validity of the relationship (Eq. (3.3)). The validity of such a simple relationship for NEMD was uncertain because of the added influence of factors such as variation in the strain rate. Consequently, we analyzed the ratio between the two ( $E_2$ ) and the three ( $E_3$ ) body potential energies obtained with planar Couette flow simulations for different state points and strain rates.

The ratio of three-body to two-body energies for argon at different densities and temperatures is shown in Figure 4.17 as a function of strain rate. The temperatures and densities represent different state points on the liquid-phase branch of the vapour-liquid coexistence curve of pure argon. Irrespective of the state point, it is apparent that the ratio of the energies is largely independent of the strain rate. The dependence of the energy ratio on density is illustrated in Figure 4.18. The values predicted by Eq. (3.3) are also illustrated for comparison. This simple relationship fits the NEMD simulation data with an average absolute deviation of 2.3%. This is close to the same quality of

agreement (2%) that was obtained for the Monte Carlo study of equilibrium properties reported in section 3.2.

As seen in the previous sections, the transport properties of fluids, such as shear viscosity, are an aspect of fluid behaviour that could potentially benefit from the use of accurate pair-potentials and three-body interactions. In common with other applications of molecular simulation, the transport properties of fluids have largely been investigated using effective potentials. Therefore, other investigations are necessary to determine if Eq. (3.3) may be used in NEMD simulations to incorporate the effect of three-body interactions without the computational cost of a full three-body calculation.

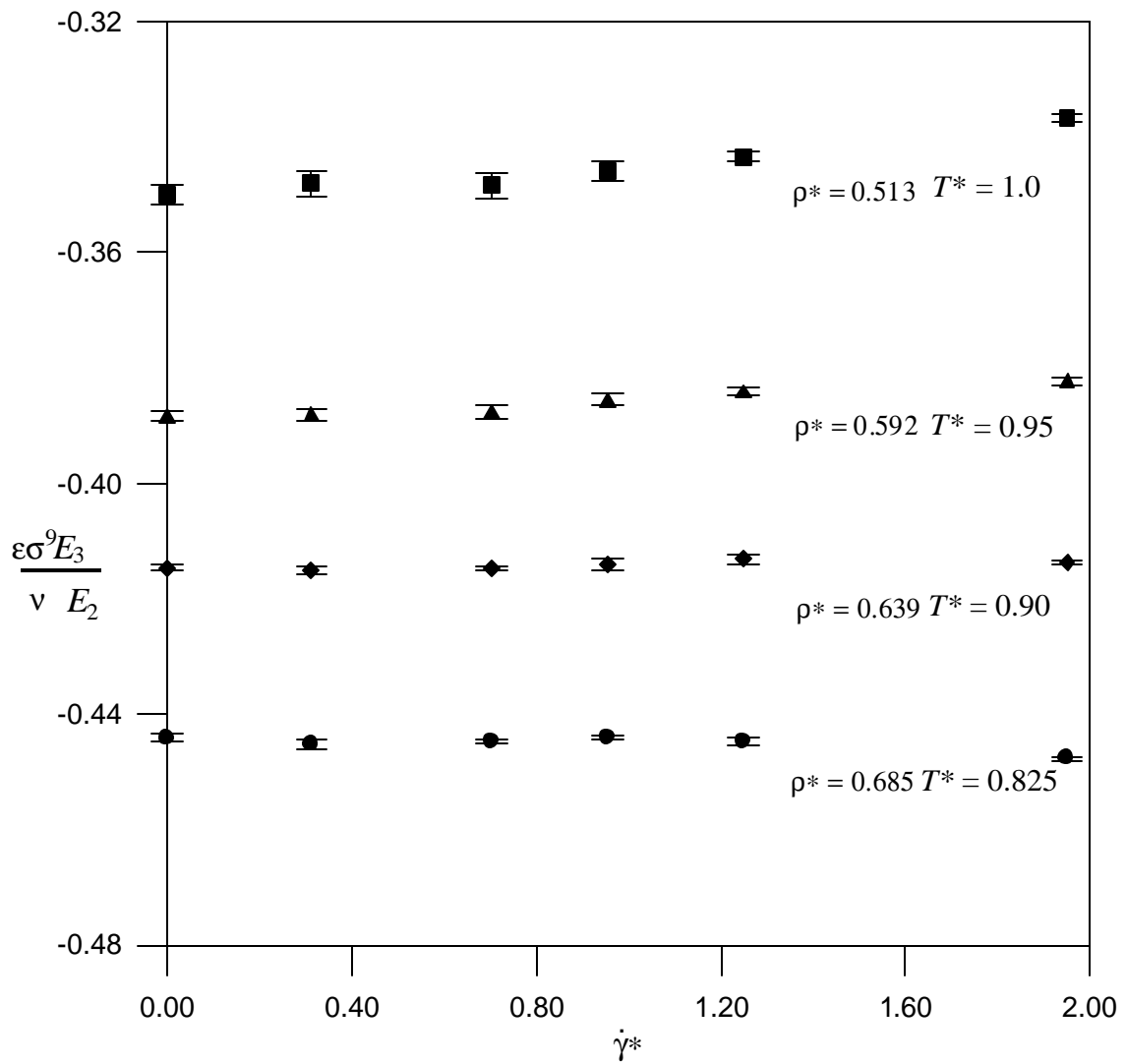


Figure 4.17 The ratio of three-body and two-body energies of argon obtained from NEMD at different state points and different strain rates.

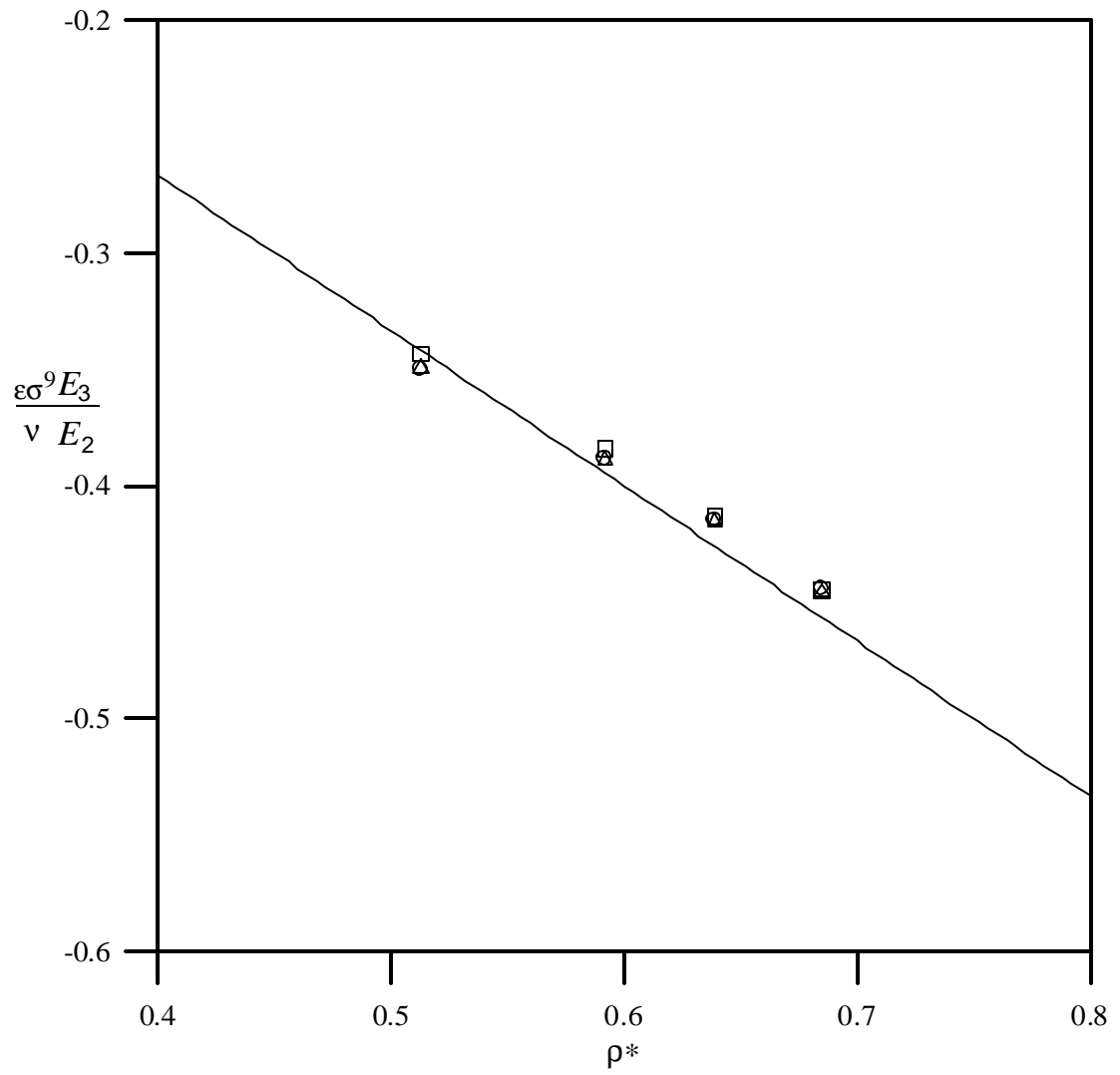


Figure 4.18. The ratio of three-body and two body energies for argon obtained from NEMD at different strain rates ( $\dot{g}^* = 0$  ( $\circ$ ), 0.702 ( $\Delta$ ), 1.428 ( $\square$ )) as a function of density. The line through the points was obtained from Eq. (3.3).